STRUCTURAL DESIGN OF AN INSTRUMENTED DOUBLE-SWEPT WIND TUNNEL MODEL

Benjamin Lütke[1*], Moritz Schmidt[2], Julian Sinske[1] and Jens Neumann[1]

[1]Institute of Aeroelasticity, German Aerospace Center (DLR)
Bunsenstraße 10, 37073 Göttingen, Germany
*Email: benjamin.luetke@dlr.de, web page: http://www.dlr.de

[2]Engineering Facility Systemhaus Technik, German Aerospace Center (DLR)
Lilienthalplatz 7, 38108 Brunswick, Germany

Keywords: Wind Tunnel Model, Finite Elements, Modal Analysis, Fluid-Structure Interaction Simulation, Strength Analysis, Helicopter Rotor Blade Tip

ABSTRACT

The design of a highly instrumented, double-swept CFRP wind tunnel model and its experimental setup are presented. A forced sinusoidal pitching motion is applied to the one-sided clamped helicopter rotor blade tip. Challenges of the structural design and the manufacturing process are addressed. A mold with inserts to check the leak-tightness of the pressure transducers and retain the half shells in the mold is presented. Insights in the finite element analysis (FEA) of the blade tip model are given. The strength analysis reveals peak stresses in the adhesive and the spar. The finite element model is validated with an experimental modal analysis. The experimental and numerical mode shapes and eigenfrequencies show an excellent agreement. The design goal of a very stiff lightweight model is met with the first eigenfrequency at 70 Hz. The results of the fluid-structure interaction simulation at Ma=0.4 show no significant differences for the global forces compared to the simulations with the rigid contour. However, the maximum tip deformation is up to 20 mm and a slight excitation of the first bending mode can be observed.

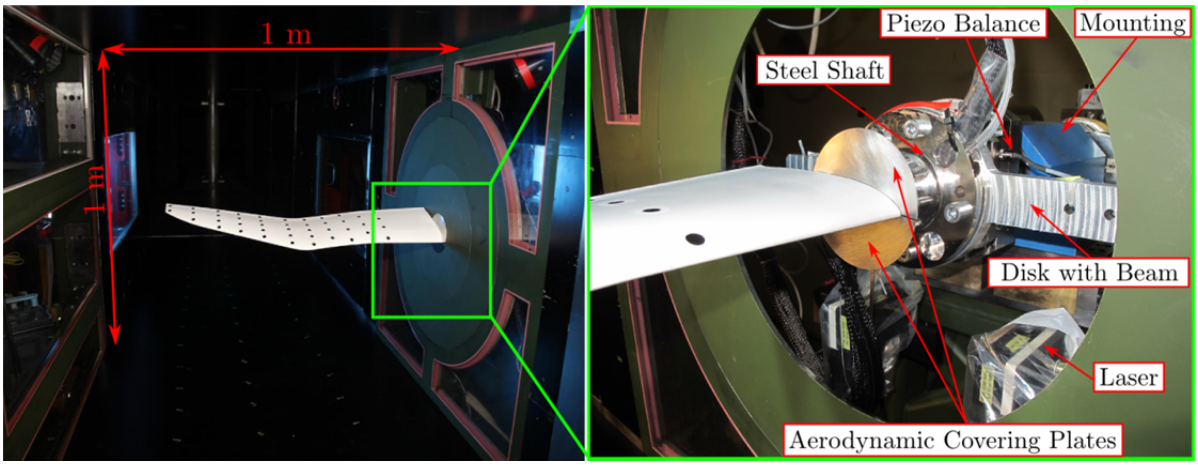

Figure 1: Model with optical markers in wind tunnel test section (left); View of installation (right)

1 INTRODUCTION

In fast forward or maneuvering flight, dynamic stall at the retreating blade of a helicopter leads to high pitching moments and can even limit the flight envelope. The dynamic stall behavior is difficult to predict and has been fully understood only for a few advanced blade tip planforms like the BERP [1]. Double swept helicopter blade tips have shown the potential to reduce noise and vibrations [2]. However, the understanding of the three-dimensional dynamic stall behavior is still limited. A new

aeroacoustically improved planform of AIRBUS-helicopters [3] is chosen for the experimental investigation in the Transonic Wind Tunnel Göttingen. In the non-rotating experiment, a forced pitching motion simulates the angle of attack variation of the once-per revolution motion of the helicopter rotor blade. This allows the influence of aerodynamic parameters on the complex flow to be investigated with high accuracy. Subsequently, computational fluid dynamic simulations (CFD) and fluid-structure interaction simulations can be validated. Comparisons to rotating cases can be made by means of simulations in a second step.

One design goal for the experimental investigation is a very stiff lightweight model in order to reduce its aeroelastic influence on the flow and limit the inertial loads. Due to a high aspect ratio with small cross sections and a high degree of instrumentation a carbon fiber reinforced plastic (CFRP) model is chosen as the best solution. Many CFRP models with more complex configurations have been presented in the past, e.g. active flaps [4]. The originality of this paper derives from the detailed insights in the structural design and the manufacturing process including instrumentation issues. The strength analysis with the high fidelity finite element model reveals the highest stress exposures in the spar due to the ribless construction. Although, the presented numerical and experimental modal analyses are standard, the importance of using the original clamp condition is striking. Correct numerical mode shapes and eigenfrequencies are essential for the fluid-structure interaction (FSI) simulations that are based on a modal approach. The presented FSI simulation at a pitching frequency of f=6.6 Hz is compared to a CFD simulation with a rigid contour.

In the first part of the paper, the experimental setup is described. In section 3, the geometry and the expected aerodynamic loads of the rotor blade tip are shown. Detailed insights into the structure and the manufacturing process are given in section 4. The finite element analysis including the numerical and experimental modal analysis is presented in section 5. Finally, a first unsteady fluid-structure interaction simulation is shown.

2 EXPERIMENTAL SETUP

The Transonic Wind Tunnel Göttingen (DNW-TWG) has a closed test section with a cross section of 1m x 1m, see Figure 1. The lower and upper wall can be adapted. Mach Numbers from Ma=0.3-0.9 are feasible. Total pressures from p_0=0.3-1.5 bar can be adjusted. A maximum temperature of T_0=323 K is expected at the model. The forced pitching motion is applied by a hydraulic test oscillation rig outside of the test section. The possible oscillation amplitude decreases for increasing pitching frequency. For sinusoidal motion the limit of the amplitude is $\alpha_{max} = 4°$ for the maximum target frequency f_{max}=13.2 Hz whereas for the target frequency f=6.6 Hz the limiting amplitude is $\alpha_{max} = 8°$. A piezo balance with four three-component piezo elements is mounted between the oscillation rig and the model in order to measure the global forces and moments. The angle of attack is measured by means of two laser triangulators pointing on a cantilever beam of an aluminum disc mounted between the model flange and the piezo balance (Figure 1). A gap of 1.5 mm between the cylindrical part of the model flange and the wind tunnel wall inserts ensures contactless operation. Aerodynamic covering plates of 0.4 mm thickness are bonded on the model flange on the inside of the wind tunnel in order to limit side flows from the plenum chamber.

Sixty unsteady pressure transducers are installed in the model to get discrete pressure data of high accuracy. The distribution of sensors is shown in Figure 2 on the left. The motion of the model is monitored by two accelerometers inside the model and by an optical marker measurement system. Two temperature sensors inside the model are used for the calibration of pressure sensitive paint, an optical measurement method which is used to receive surface pressure information in the experiment. The sensor systems described above have to be considered in the design phase with regard to space for instrumentation and cable feedthrough.

3 GEOMETRY OF THE WIND TUNNEL MODEL AND EXPECTED AERODYNAMIC LOADS

A maximum span s=750 mm is chosen in order to limit the aerodynamic interference of wind tunnel wall and tip vortex. The planform, shown in Figure 2, is adapted from a parametrized AIRBUS-HELICOPTER patent [3].

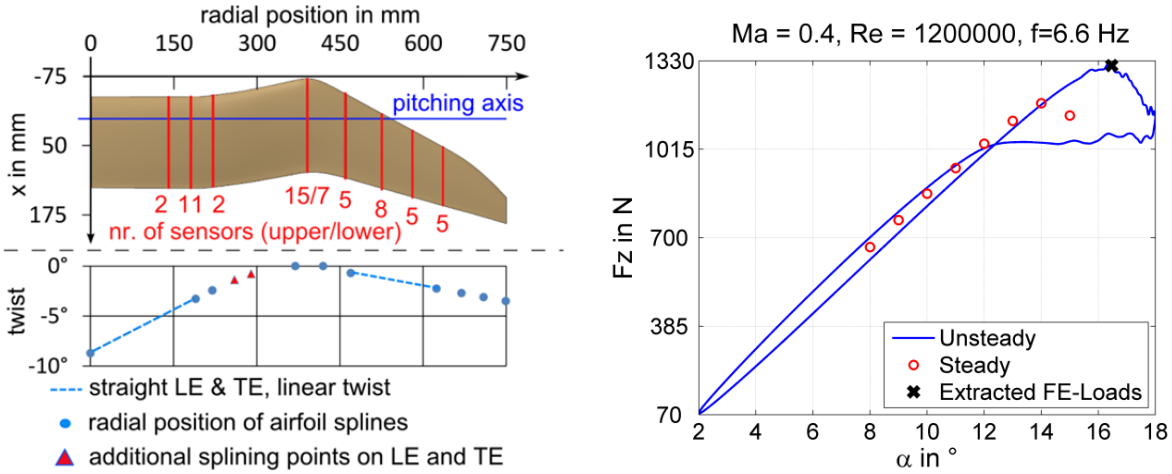

Figure 2: Planform, twist and sensor distribution from [5] (left); Aerodynamic load case (right)

A high aspect ratio of AR=4.5 is required to resolve flow separation at high angles of attack inboard of notch. The forward sweep of $\Lambda \approx 11°$ begins at r=200 mm and ends at r=390 mm. The chord length (c=165 mm) is nearly constant until the latter position. With the beginning of the backward sweep of $\Lambda \approx 25.7°$ the chord length linearly decreases to c=106 mm at r=638 mm. The parabolic tip shape leads to a minimal chord length of c_{min}=47.5 mm at the tip. The model has no anhedral in order to reduce optical measurement complexity. The twist distribution of a realistic helicopter rotor blade usually decreases from the root to the tip due to the varying inflow velocity along the blade. The twist distribution of the wind tunnel model, as shown in Figure 2, is decreased at the root so that the first separation inboard of the notch is not triggered by the wind tunnel wall separation.

The airfoil EDI-M112 with 12% thickness is used for the inner unswept part while the airfoil EDI-M109 with 9% thickness is used for the forward/backward swept part [5]. Consequently, the maximal thickness of the blade is 16 mm. The trailing edge of the outer part is thickened to allow a minimum thickness of t_{min}=0.5 mm.

A typical unsteady aerodynamic load case at Ma=0.4 and Re=1200000 is shown in Figure 2 on the right. The unsteady CFD-simulation with rigid contour leads to a maximum lift force of F_Z=1313 N whereas the steady lift peak remains at F_Z=1180 N. Therefore, the maximum loads of the unsteady simulation are used for the strength analysis presented in Section 5.3. Besides the calculation of the global loads, the aerodynamic flow phenomena are investigated by means of the CFD-simulation, see [6].

4 STRUCTURAL COMPONENTS AND MANUFACTURING OF THE CFRP-MODEL

Several requirements lead to a carbon fiber reinforced plastic design of the wind tunnel model:

- The high bending and torsional stiffness needed to limit the aeroelastic influence on the flow
- A lightweight construction for low inertial loads due to the forced motion
- The high aspect ratio which leads to a small chord length and reduces the space for instrumentation and cable feedthrough.

The two CFRP half shells with integrated spar caps, shown in Figure 3 on the right, carry the main bending loads. One central spar resists shear forces and prevents buckling. Torsional loads are carried by the closed shell and the central spar. A hollow steel shaft is adhesively connected to the shells and the spar at the model root and transfers the loads to the hydraulic oscillation rig (Figure 1). Vacuum bag molding is used for all composite parts of the model.

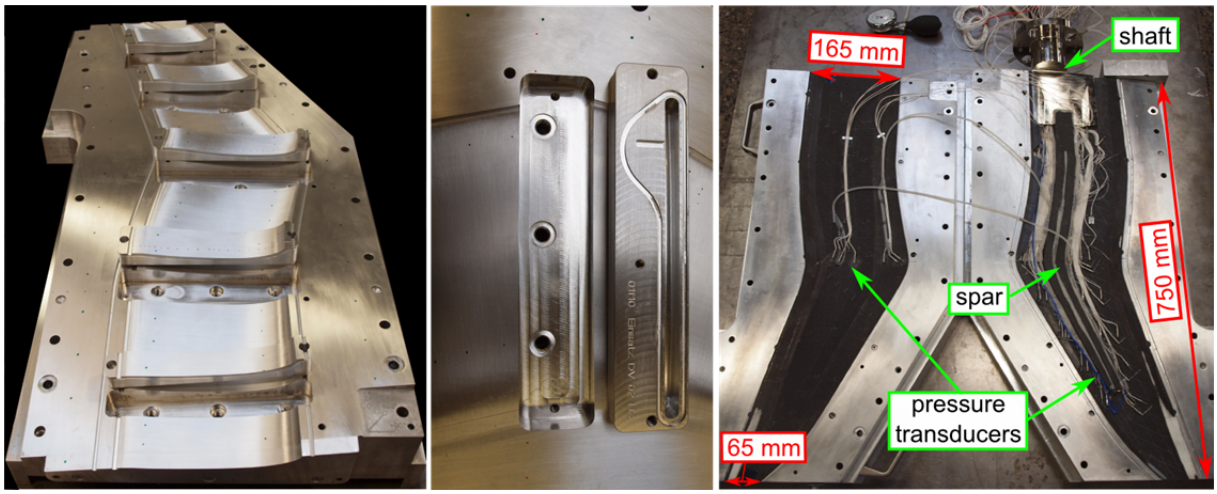

Figure 3: Aluminium mold with removable inserts (left, mid); Full instrumented half shells (right)

The upper and lower half shell are hand layed in the aluminum molds shown in Figure 3 on the left. The high surface quality with $R_z < 3$ µm along with the robustness and the reusability compensate the high costs of the mold. Each mold has five hollow, removable inserts which are distributed along the wingspan including the main instrumented sections. Thus, the holes for the discrete pressure measurements with a diameter $\emptyset = 0.3$ mm can be drilled from the half shell through the inserts. Due to the cavity of the inserts, the pressure transducers are not destroyed by overpressure when inserting them into the brackets (Figure 4). Furthermore, the leak-tightness can be tested during the manufacturing process. In case of an unwanted detachment of the half shells the inserts can be removed from the mold while the half shells are retained in the mold by partial vacuum for the final bonding process.

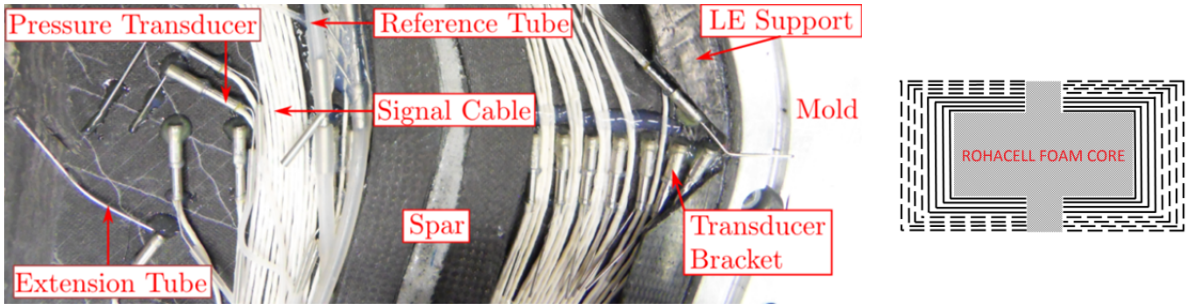

Figure 4: Detail of instrumentation at the notch (left); Sketch of spar cross section (right)

The high modulus, unidirectional M46J-lamina and the epoxy LR385 are used for the half shells. In order to avoid dry spots, a maximum fiber volume fraction of 50% is chosen for the complex geometry. The symmetric ply layout is listed in Table 1. Ply 7-18 are the integrated spar caps which are orientated 2.5° in forward direction in order to follow the spar contour and enforce the bending-torsion coupling. The spar caps have a chordwise tapering of 8:1 and taper out right behind the notch. The approximate position of the spar caps is shown in Figure 10 on the left. A spanwise tapering of 26:1 is used at the steel shaft to reduce stress concentrations and transfer loads smoothly from the half shells to the steel shaft. Plies 3-4 and 21-22 are dropped at the beginning of the parabolic tip since loads decrease in tip direction and instrumentation space is limited due to the tapered geometry. The first and the last six plies as well as the integrated spar caps are laminated in separate steps. The fiber volume fraction is met precisely to ensure strength and the correct thickness for perfect integration of spar and steel shaft. An adhesive gap of 0.4 mm between the components is not exceeded. The holes

for the pressure transducers and the corresponding brackets are drilled before the other parts are glued to the half shells.

Table 1: Layup of upper and lower half shell at position of integrated spar caps – HM lamina M46J

Layer	1	2	3	4	5	6	7-18	19	20	21	22	23	24
Orientation in °	-45	45	90	0	23	-23	-2.5	-23	23	0	90	45	-45

The contour of the central spar follows the contour of the blade tip. The milled foam core (ROHACELL) is covered with two C-shapes ±45° weave Style469, see Figure 4. The C-shapes of the weave end right before the heightening of the foam core which indicates the thickness limit of the spar for optimal integration into the half shells. An exact fiber volume fracture of =50% is difficult to meet since the weave is not easy to be fixed on the core with its small dimensions and radii. Only one pressure transducer is placed at the position of the spar to not weaken the weave. A notch is cut in the foam core and the weave is laminated along this notch. The spar has an upper and lower overlap to the steel shaft for a more homogeneous stress distribution. The upper overlap is laminated on the spar by means of a plastic support construction. After the spar with the upper overlap is bonded to the upper shell, the steel shaft is glued in place. Then, the lower overlap is laminated on the spar and the steel shaft. Before the pressure transducer brackets are glued in the half shells with epoxy, the leading edge (LE) support structure is glued in the upper shell. Cut outs at the positions of the transducers and the brackets are provided. The pressure transducers are glued in the brackets with silicone due to its vibration resistance. Silicone is also used to fix the cables and transducers in the half shells (Figure 4).

For the LE support structure, a support shell is laminated in the front part of one original aluminum mold. A carbon half mold is laminated on the outer contour of this support shell and connected to the other original aluminum mold. Finally, the LE support structure is laminated to the U-contour of the original aluminum mold and the connected carbon front mold. The original specified weave “Style 452 - T 700 SC” could not be used neither for the weave of the spar nor for the LE support structure because it turned out to be too stiff to fit on the small radii during laminating.

The steel shaft is milled of a 42CrMo4 steel block. It has one main channel for cable feedthrough and one spanwise and chordwise channel in order to reduce stress concentrations and save weight. Milled slots are provided for the spar overlap. The steel shaft is fixed with 4 M10 screws to a distance disk with cantilever beams where the angle of attack is measured with two laser triangulators, see Figure 1. Two hole patterns are provided for different angles of incidence. The distance disk is fixed with 16xM6 screws to the Piezo balance on the hydraulic test oscillation rig so that the forces are homogeneously distributed to the 4 Piezo elements. An external centering is provided between the steel shaft and the disc, an internal centering between balance and disk.

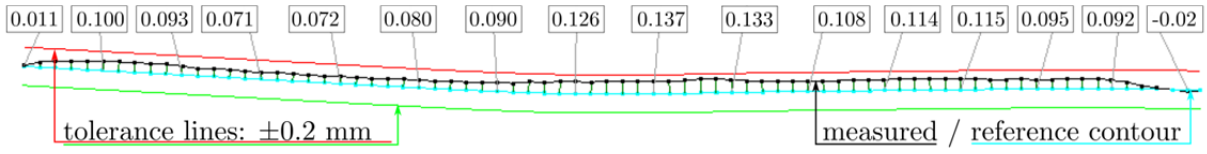

Figure 5: Spanwise measured deviation: upper surface 15 mm in front of the TE, resolution: 10 mm

After the final bonding procedure, the model is cured for 15 hours at 55°C. The surface contour shows a slight thickening of about 0.1 mm compared to the reference contour. One measured spanwise cross section of the upper surface is shown in Figure 5. However, no signs of the inserts of the mold can be seen.

5 FINITE ELEMENT ANALYSIS AND VERIFICATION

A high-fidelity finite element model based on a linear approach is established in ANSYS-APDL. The unsteady CFD-load case at Ma=0.4 and Re=1200000, see Figure 2, is used for the strength analysis presented hereafter. The experimental modal analysis is compared with the numerical results to verify the finite element model and to define possible adaptions to the finite element model.

5.1 FE Modeling

Four different element types are used for the finite element model: the 8-node layered shell element SHELL281, the 20-node solid element SOLID186, the 2-node beam element BEAM188 and the rigid region link CERIG [7].

In Figure 6 the modeling is shown in detail: the laminate of the half shells, the leading edge support structure and the weave cover of the spar are modeled with layered shell elements. The steel shaft, the foam core of the spar and the adhesive are modeled with solid elements.

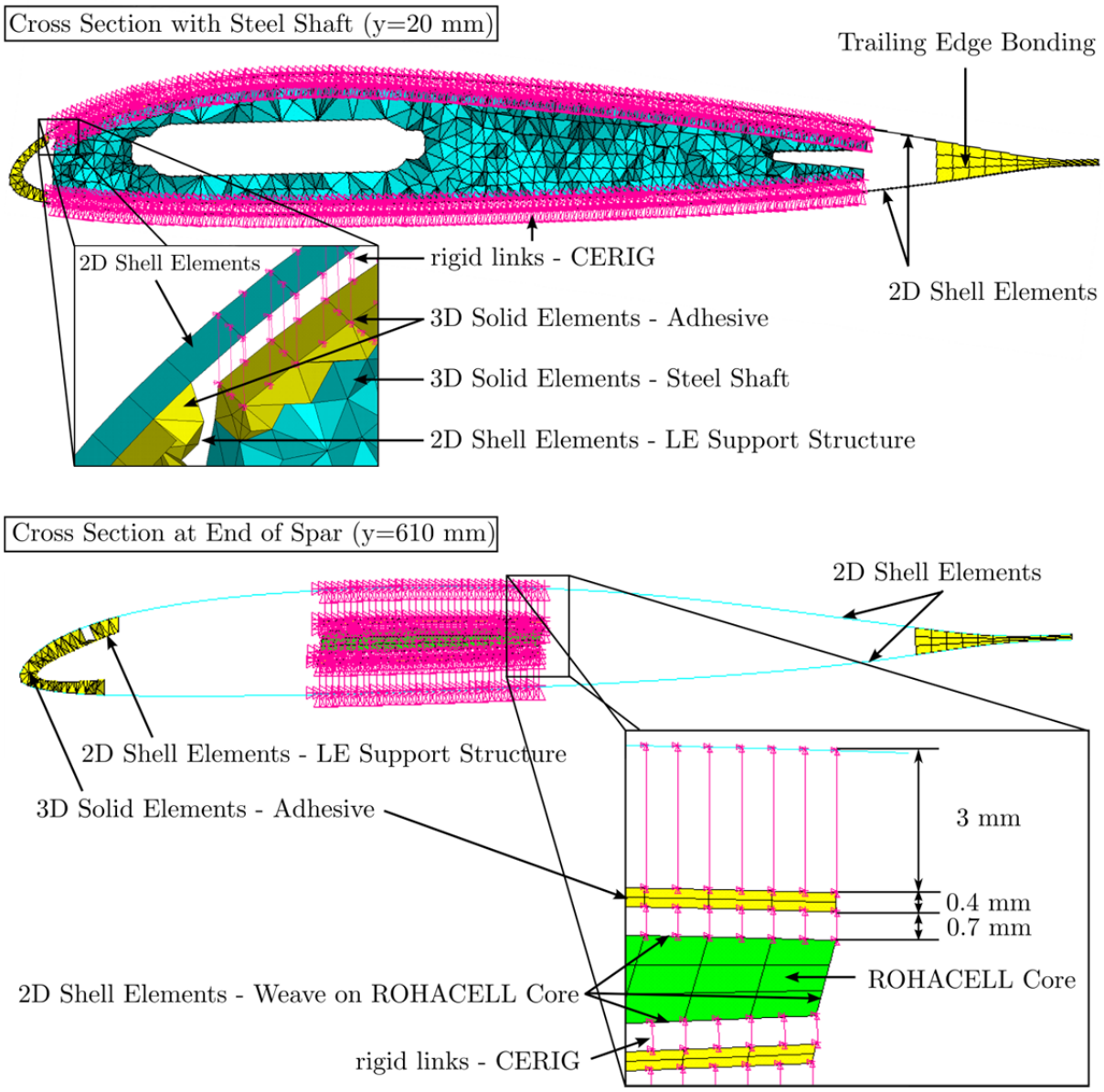

Figure 6: Finite element modelling of the wind tunnel model (distorted illustration of the airfoils)

Different modeling approaches for the adhesive and the connection between solid and shell elements have been presented in [6]. In the final modeling approach presented in this paper, the structured shell elements simulating the upper and lower half shell are placed on the outer contour. The t=0.3 mm thick adhesive between the steel shaft and the half shells is modeled with solid elements. The elements are placed on the faces of the unstructured solid elements of the steel shaft. The free faces of the adhesive on the opposite site of the half shells are structured and have the same node distribution as the structured elements on the half shells. The nodes are linked by CERIG-elements with the length of the final laminate thickness.

The structured shell elements simulating the weave of the spar are placed on the faces of the structured solid elements simulating the foam core. The opposite nodes of the solid elements representing the adhesive are linked to the nodes of the spar via a distance equal to the weave thickness t=0.7 mm by CERIG elements. The nodes on the other side of the t=0.4 mm thick adhesive are linked to the nodes of the half shell elements by CERIG elements.

The leading edge support structure is modeled with shell elements which are connected to the shell elements of the half shells by solid elements, with the property of the adhesive. This leads to an overrated bonding thickness which reduces stress peaks in the adhesive.

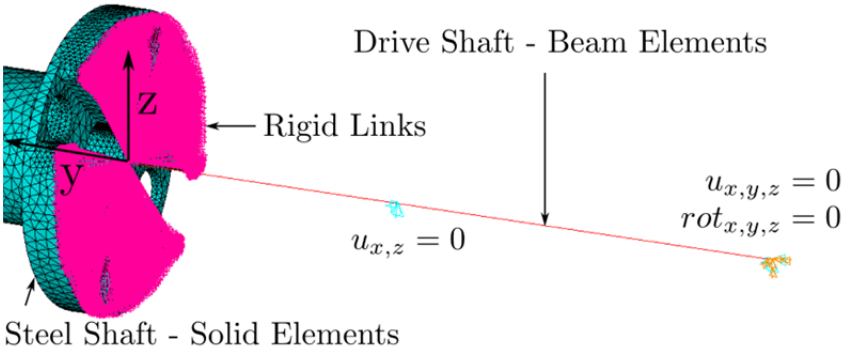

Figure 7: FE - modeling of boundary conditions wind tunnel boundary condition

The wind tunnel clamp is modeled with beam elements which have the material properties of steel, see Figure 7. At the position of the bearings the nodes are fixed: one is simulated as a fixed bearing with all degrees of freedom fixed, the other is simulated as a floating bearing with fixed displacements in x- and z-direction. The cross section of the beam elements reflects the cross section of the driving axis. However, the disc with the cantilever beam (Figure 1) is not included in the FE model. Furthermore, the rigid links between the last beam element and the solid elements of the steel shaft might lead to a too stiff behavior of the numerical model. Thus, the modeling shown in Figure 7 is rather a rough approximation of the real boundary condition.

5.2 Numerical and experimental modal analysis

The numerical and experimental modal analyses are performed with two different boundary conditions. The first is the clamped condition in the wind tunnel, shown in Figure 1 and Figure 7. The experimental part of this modal analysis is done hours before the wind tunnel experiment starts, so these data cannot be used for a finite element model validation which supports the strength analysis required for the wind tunnel test. The second is the model clamped to a solid steel block, as shown in Figure 8. In this setup the model is easily excited with either a shaker or with an impact hammer. This experimental modal analysis is used for the finite element model validation a long time before the wind tunnel experiment.

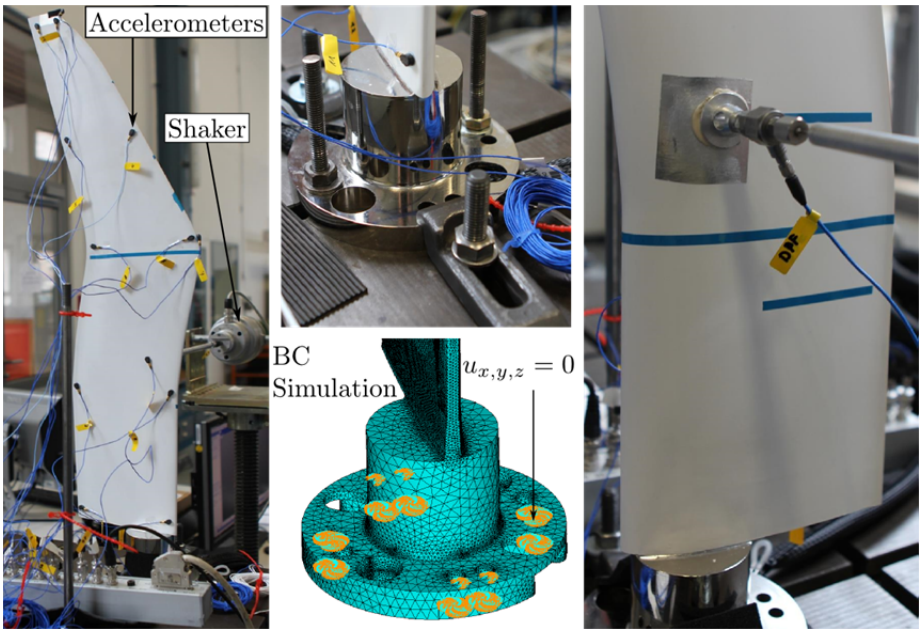

Figure 8: Experimental modal analysis on a solid steel block and FE modeling of boundary condition

The experimental results, presented in Table 2 and Figure 9, are produced by means of the impact hammer. The clamped support of the wind tunnel on the one hand and the steel block on the other hand explain the differences between the eigenfrequencies corresponding to the two boundary conditions. The stiffer clamped support of the steel block leads to higher eigenfrequencies in general. The realistic FE-modelling of the boundary conditions shown in Figure 8 leads to good agreements between the numerical and experimental results in case of the steel block. The modal assurance criterion (MAC) is greater than 93% for the first four mode shapes and even the 6th mode shape has a MAC-value of 78%. For the comparison of the numerical and experimental mode shapes the correlation coefficient presented in [8] is used. The results might be further improved by integrating the masses of sensors and cables. The discrepancies between the numerical and experimental results in case of the wind tunnel clamp are due to the imprecisely simulated model connection. However, these modes reflect the experimental wind tunnel clamp condition better than the fixed boundary condition in case of the steel block, shown in Figure 8. Therefore, they are used for the first fluid-structure coupled interaction simulation.

Table 2: Experimental and numerical eigenfrequencies for different boundary conditions

Mode Number		1	2	3	4	5	6
Numerical Frequency in Hz	Clamp Steel Block	69.4	198	299	429	499	752
Experimental Frequency in Hz		69.6	196	275	434	463	729
Numerical Frequency in Hz	Clamp Wind Tunnel	67.7	181	201	369	430	530
Experimental Frequency in Hz		67.3	153	186	273	466	515

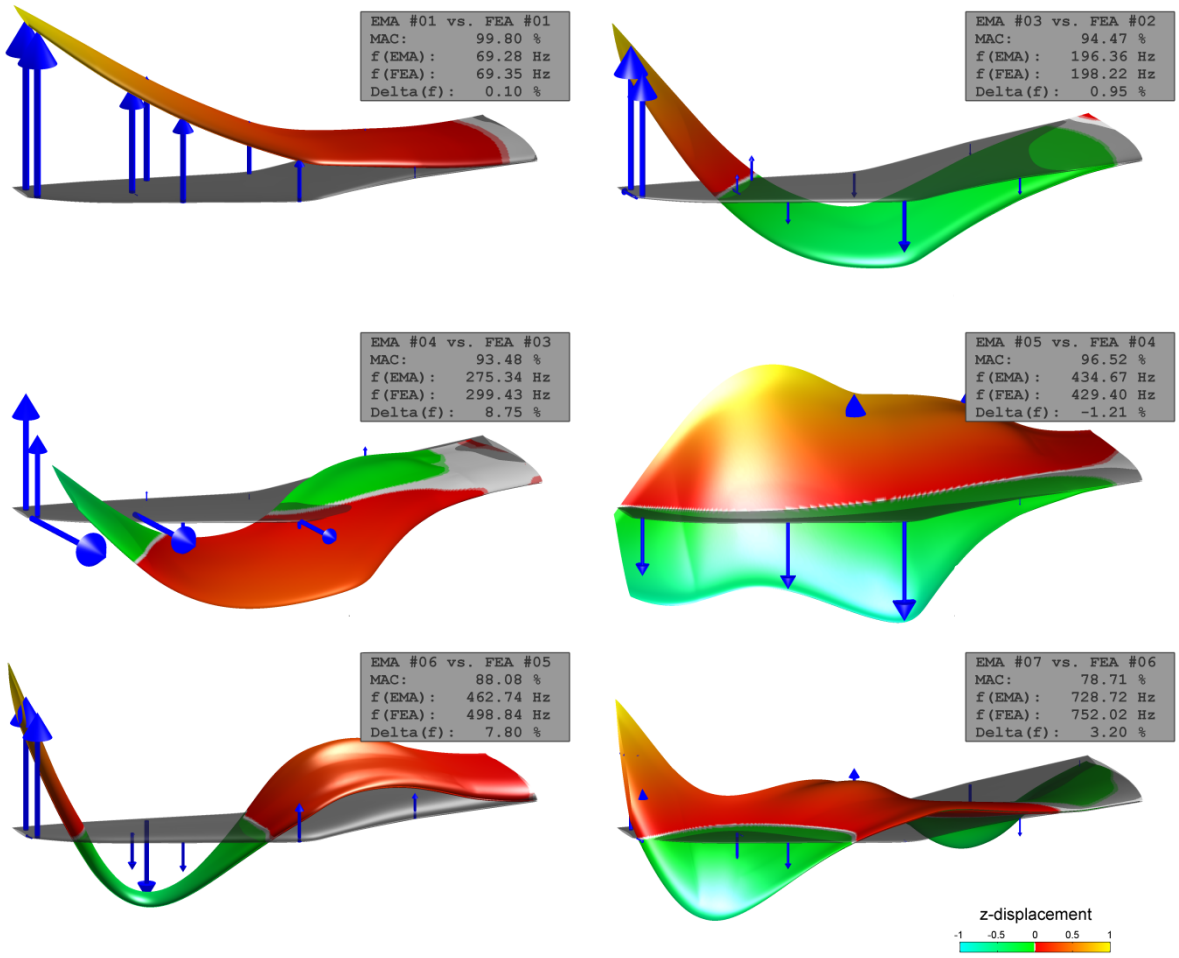

Figure 9: Experimental (blue arrows) and numerical (surface solution) results of the modal analysis

5.3 Strength Analysis

For the strength analysis, unsteady CFD-simulations with a rigid contour are carried out. The load cases with the estimated highest loads are simulated and chosen for the strength analysis. The loads at the point of the highest lift are extracted and applied statically on the finite element model. The solution is superposed on the harmonic analysis. In the harmonic analysis the harmonic motion is applied on the model only. The procedure and details of the CFD-simulations are described in [6]. The loads are interpolated from the CFD grid to the FEM grid by means of radial basis functions. The load case used for the strength analysis presented in the following is shown in Figure 2. The model is exposed to a forced pitching motion (f=6.6 Hz, α=10 $\pm$ 8°) at Ma=0.4 and Re=1200000. The loads are extracted at the instantaneous angle of attack α_{inst}=16.47°.

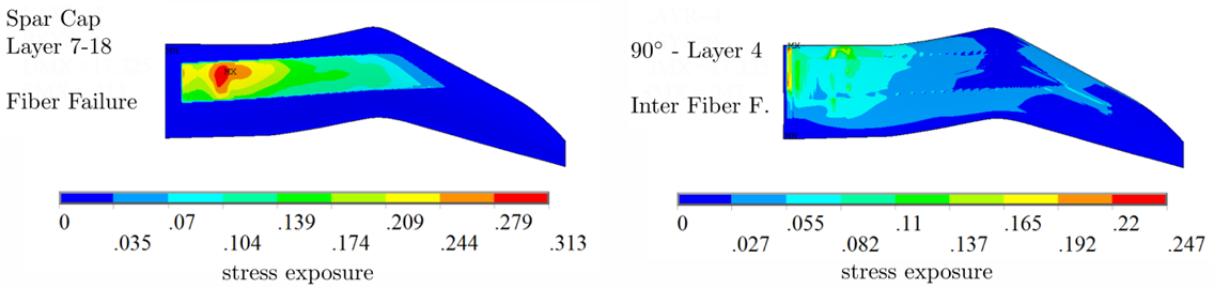

Figure 10: Stress exposure: FF - upper shell (left); IFF – lower shell (right)

For the strength analysis of the half shells the Puck criterion [9] is used. It identifies fiber failure (FF) and inter-fiber failure (IFF) in the unidirectional M46J lamina listed in Table 1. The out-of plane properties of the M46J lamina and the four Puck inclination parameters are estimated with data from similar materials while the other material properties are determined experimentally. The upper half shell is more critical to fiber failure then the lower half shell since the compressive strength in fiber direction is approximately half as much as the tensile strength. The highest physical relevant stress peaks occur at the spanwise end of the steel shaft in the 0°-2.5°-layers. The stress exposure of the spar cap layers is shown in Figure 10. Higher numerical stress exposures can be found in the first +45° layer due to the modeling discontinuities in the tapering. Therefore, these stress peaks can be considered lower in reality. Nevertheless, the safety margin has a conservative value of S=2.6. The lower half shell is most critical to inter-fiber failure in the 90° layers due to negative influence of the orthogonal tension on inter-fiber failure, as in Figure 10. The safety margin of IFF is S=4.0.

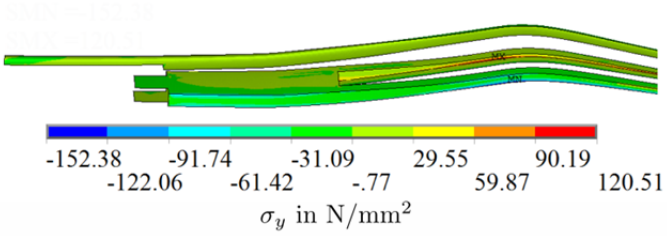

Figure 11: Stress σ_y in shell elements simulating the weave of the LE support structure and the spar

The maximum stress criterion is used for the elements simulating the "Style 469 – T 300" weave. The material properties of the "Style 469 – T 300" weave are adapted from the experimentally determined properties of the weave "Style 452 - T 700 SC" and other laminates based on the T 300 fiber. The maximum stresses are listed in Table 3. The highest stress exposure or the lowest safety margin S=2.47 occurs for compressive pressure in fiber direction, shown in Figure 11. The stress is highest at the position of the notch where most of the pressure transducers are located. Since the corner radii of the core are not taken into account, the stress peaks are lower in reality. The same holds for the shear stresses in the bonding on the upper and lower side of the spar, shown in Figure 12.
Therefore, one can assume that the required safety margin S=2 is met assuming a maximum mean shear stress of $\tau_{yz,max}$=7 MPa for the adhesive.

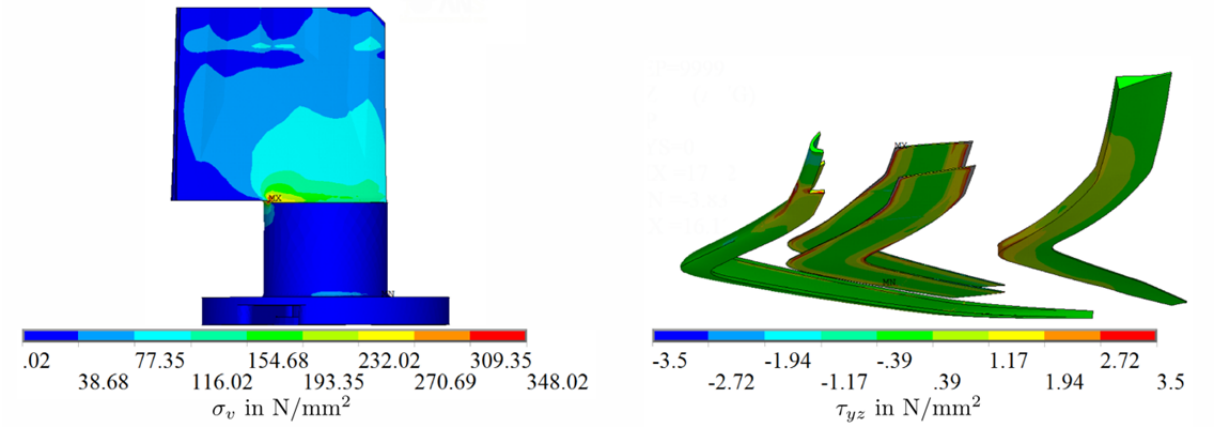

Figure 12: Von-Mises stress in steel shaft (left); Shear stress τ_{yz} in bonding, global coordinates (right)

The mean shear stress in the bonding on the upper side of the shaft is calculated by the simple formula

$$\tau_{yz} = \frac{F}{A} = \frac{18873\ N}{15000\ mm^2} = 1.26\ N/mm^2$$

where F are the internal section forces in spanwise direction summed over the nodes of the upper shells and A is the upper surface area of the steel shaft. The maximum mean shear stress divided by the mean shear stress of the shaft yields a safety margin of S=5.6.

Table 3: Maximum stresses used for the weave "Style 469 – T 300"

R_x^+	R_x^-	R_{xy}
$690\ N/mm^2$	$376\ N/mm^2$	$80\ N/mm^2$

The von-Mises criterion is applied to the foam core and to the steel shaft, shown in Figure 12. The highest stresses are on the transition to the cylindrical part of the steel shaft. Numerical singularities occur at the 90°-corners of the shaft. Nevertheless, the safety margin is S=2.87.

6 FLUID-STRUCTURE INTERACTION SIMULATIONS

The setup and the procedure for steady fluid-structure interaction simulation (FSI) are described in [6] and [10]. The unsteady simulation restarts from a converged steady-elastic solution. The simulation has 500 physical timesteps per period and up to 1000 inner iterations per timestep depending on a Cauchy convergence criterion.

The steady FSI, shown in [6], revealed no significant differences to the simulations with the rigid contour regarding the global forces. In Figure 13 only negligible differences in the lift coefficient between the unsteady FSI case and the CFD-simulation with a rigid contour are visible. The lift coefficient over one period, starting the downstroke from the mean angle of attack, is shown on the left. The maximum elastic tip deformation is about 20 mm at the point of the highest lift. The Fourier-transformation of the deformation signal shows the 10th higher harmonic frequency at 66 Hz slightly elevated in comparison to the neighbour frequencies. This might be due to an excitation of the first bending frequency of 67.7 Hz.

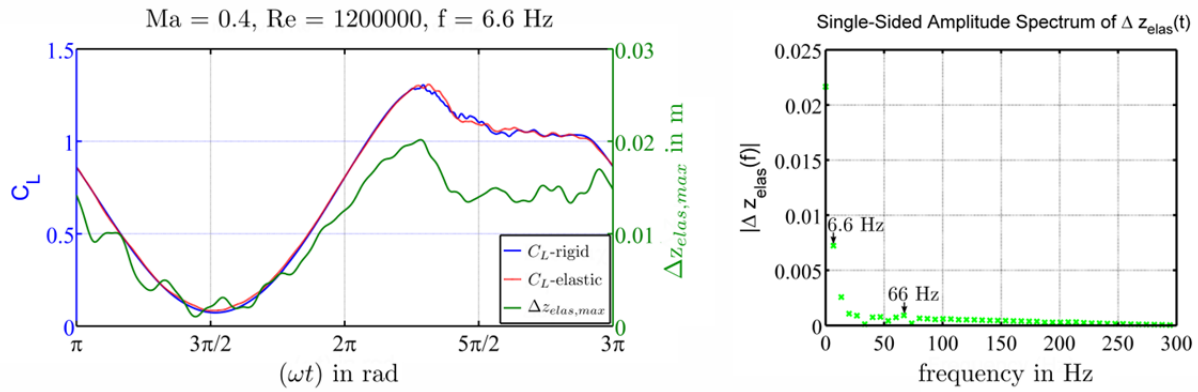

Figure 13: Lift and tip deformation in one period: $\alpha = 10° + 8° \cdot \sin(\omega t)$ (left); FFT of Δz_{elas} (right)

7 CONCLUSIONS

The structural design of a double-swept rotor blade tip for the investigation of dynamic stall in the Transonic Wind Tunnel Göttingen is presented in this paper.

- The ribless CFRP model can be used as a guideline for highly loaded wind tunnel models with a high degree of instrumentation. The concept of one central spar simplifies cable feedthrough and assures high stiffness and stability. A strength analysis exhibits the highest stress peaks in the spar and the adhesive. Furthermore, stress concentrations occur at the stiffness discontinuities of the root and the spanwise end of the steel shaft.
- A mold with inserts or possibilities to check the leak-tightness of the pressure transducers is recommended. The presented mold has the possibility to retain the half shells in the mold by partial vacuum in case of an unwanted detachment.
- The experimental modal analysis on a solid steel block shows excellent agreements to the numerical results. However, the experimental and numerical results with the wind tunnel clamp condition show discrepancies due to the simplified boundary condition in the FE model.
- The fluid-structure interaction simulation at Ma=0.4 and Re=1200000 shows no significant differences in the global loads compared to the CFD-simulations with the rigid contour. Thus, the strength analysis based on the load case with the rigid contour is considered sufficient.

Further FSI-simulations should hence be carried out with an improved clamp condition in the finite element model. Finally, these simulations should probably show good agreements with the experimental wind tunnel results.

ACKNOWLEDGEMENTS

The author would like to thank M. Müller, S. Roth and R. Winters for the manufacturing of the wind tunnel model. The author would like to thank N. van Hinsberg, S. Sedlmair and Y.M. Meddaikar for paper correction. The work is founded by the DLR programmatic research in the project STELAR.

REFERENCES

[1] M. T. Scott, S. Dave and R. C. Strawn, Computational and Experimental Evaluation of Helicopter Rotor Tips for High Speed Forward Flight, *Journal of Aircraft,* vol. 89, pp. 403-409, 1991.

[2] P. Rauch, M. Gervais, J.-F. Hirsch, A. Baud und P. Beaumier, Blue Edge: The Design, Development and Testing of a New Blade Concept, *AHS 67th International Forum,* 2011.

[3] D. Schimke, S. Link und S. Schneider, Noise and performance improved rotor blade for a helicopter. Patent EP 2 505 500 A1, 03 2011.

[4] S. Opitz, A. D. Gardner und . K. Kaufmann, Aerodynamic and structural investigation of an active back-flow flap for dynamic stall control, *CEAS Aeronautical Journal,* pp. 279-291, 5 2014.

[5] A. Gardner, K. Richter, H. Mai, A. Altmikus and A. Klein , Experimental investigation of dynamic stall performance for the EDI-M109 and EDI-M112 airfoils, *Journal of the American Helicopter Society,* vol. Vol. 58, no. No. 1, p. pp. 1–13, 2013.

[6] B. Lütke, J. Neumann und M. Schmidt, Design of a Rotor Blade Tip for the Investigation of Dynamic Stall in the Transonic Wind Tunnel Göttingen, in *European Rotorcraft Forum*, Southampton, 2014.

[7] ANSYS, *ANSYS Mechanical APDL Theory Reference,* 2012.

[8] R. J. Allemang, The modal assurance criterion–twenty years of use and abuse, *Sound and vibration ,* Bd. 37.8 , pp. 14-23, 2003.

[9] A. Puck, Failure analysis of FRP laminates by means of physically based phenomenological models, *Composites Science and Technology,* Bd. 58, Nr. 7, pp. 1045-1067, 1998.

[10] J. Neumann and H. Mai, Gust response: Simulation of an aeroelastic experiment by a fluid-structure interaction method, *Journal of Fluids and Structures,* vol. 38, p. 290–302.